Global and Planetary Change 164 (2018) 52–64

Contents lists available at ScienceDirect

Global and Planetary Change

journal homepage: www.elsevier.com/locate/gloplacha

Novel sedimentological fingerprints link shifting depositional processes to Holocene climate transitions in East Greenland

Willem G.M. van der Bilt[a,b,*], Brice Rea[c], Matteo Spagnolo[c], Desiree L. Roerdink[a,d], Steffen L. Jørgensen[a,d], Jostein Bakke[a,b]

[a] Department of Earth Science, University of Bergen, Allégaten 41, 5007 Bergen, Norway
[b] Bjerknes Centre for Climate Research, Bergen, Norway
[c] School of Geosciences, University of Aberdeen, Elphinstone Road, Aberdeen, Scotland
[d] K.G. Jebsen Centre for Deep Sea Research, Bergen, Norway

ARTICLE INFO

Keywords:
Arctic
Lake sediments
Paleoclimate
Glacier change
CT scanning

ABSTRACT

The Arctic warms faster than any other region of our planet. Besides melting glaciers, thawing permafrost and decreasing sea-ice, this amplified response affects earth surface processes. This geomorphological expression of climate change may alter landscapes and increase the frequency and magnitude of geohazards like floods or mass-movements. Beyond the short span of sparse monitoring time series, geological archives provide a valuable long-term context for future risk assessment. Lake sediment sequences are particularly promising in this respect as continuous recorders of surface process change. Over the past decade, the emergence of new techniques that characterize depositional signatures in more detail has enhanced this potential. Here, we present a well-dated Holocene-length lake sediment sequence from Ammassalik Island on southeast Greenland. This area is particularly sensitive to regional shifts in the Arctic climate system due to its location near the sea-ice limit, the Greenland Ice Sheet and the convergence of polar and Atlantic waters. The expression of Holocene change is fingerprinted using physical (grain size, organic content, density), visual (3-D Computed Tomography) and geochemical (X-Ray Fluorescence, X-Ray Diffraction) evidence. We show that three sharp transitions characterize the Holocene evolution of Ymer Lake. Between 10 and 9.5 cal. ka BP, rapid local glacier loss from the lake catchment culminated in an outburst flood. Following a quiescent Holocene climatic optimum, Neoglacial cooling, lengthening lake ice cover and shifting wind patterns prompted in-lake avalanching of sediments from 4.2 cal. ka BP onwards. Finally, glaciers reformed in the catchment around 1.2 cal. ka BP. The timing of these shifts is consistent with the regional expression of deglaciation, Neoglacial cooling and Little Ice Age-type glacier growth, respectively. The novel multi-proxy approach applied in this study rigorously links depositional sediment signatures to surface processes and thereby provides a key step towards a process-based understanding of climate responses.

1. Introduction

The Arctic currently warms almost twice as fast as the planet as a whole (Jeffries et al., 2015). Yet despite the global ramifications of this regional response (e.g. sea-level rise), we do not fully understand the causes and consequences of the Arctic amplification of climate change through time (Serreze and Barry, 2011). Paleoclimate data helps us advance this debate by providing a long-term context for the behavior of the Arctic climate system (Sundqvist et al., 2014 and references therein). Characterized by similar large-scale boundary conditions like ice-sheet extent, sea level and land configuration (e.g. Wanner, 2014), the Holocene provides a highly relevant baseline to understand ongoing and near-future climate change (Marcott et al., 2013).

Although the number of Holocene Arctic paleoenvironmental studies has increased over recent years, records remain few and far between and chronological control is often poor (Sundqvist et al., 2014). Clearly, there is a need for well-dated and strategically located proxy records to resolve the spatio-temporal dynamics of Holocene Arctic change. As continuous recorders of change that are widely distributed across the region (Lamoureux and Gilbert, 2004a), lacustrine sediment sequences are well-positioned to address this pressing issue. In lake sediments, a profusion of physical, magnetic, geochemical and biological properties record different aspects of terrestrial environmental change (Last and Smol, 2002). In the Arctic, the imprint of variability is

* Corresponding author at: Department of Earth Science, University of Bergen, Allégaten 41, 5007 Bergen, Norway.
E-mail address: willemvanderbilt@uib.no (W.G.M. van der Bilt).

https://doi.org/10.1016/j.gloplacha.2018.03.007
Received 1 December 2017; Received in revised form 9 March 2018; Accepted 13 March 2018
Available online 19 March 2018
0921-8181/ © 2018 Elsevier B.V. All rights reserved.

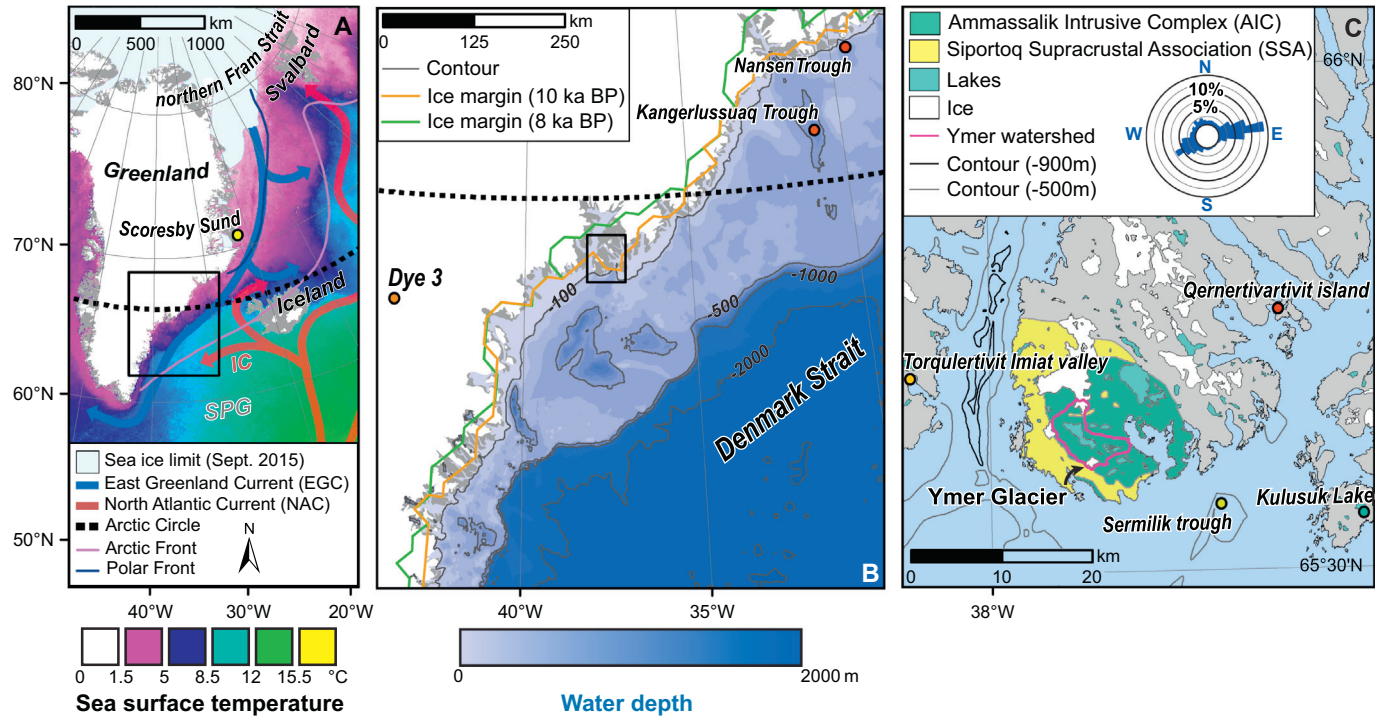

Fig. 1. A: overview map of Greenland and the western sector of the North Atlantic Ocean, showing September 2015 sea-ice extent (Fetterer et al., 2016), 1985–2009 average annual Sea Surface Temperatures (SST)(NOAA, 2012), Polar and Arctic fronts as well as major ocean currents - highlighting the Irminger Current (IC) and Subpolar Gyre (SPG) - modified after Alonso-Garcia et al. (2011). B: close-up of the southeast Greenland coast, indicating bathymetric contours (Dorschel and Jakobsson, 2016), as well as the present extent of the Greenland Ice Sheet (GIS) (CEC, 2004), while highlighting its reconstructed extent between 10 and 8 ka BP after Lecavalier et al. (2014). C: inset of Ammassalik Island, displaying the distribution of bedrock, glaciers, lakes and fjord bathymetry after Schjøth et al. (2012) and (Kolb, 2014). The pink line delimits the Ymer lake watershed. An arrow points at Ymer Glacier. The blue rose diagram in the legend displays the frequency of wind directions for the 2006–2010 period (Gelaro et al., 2017). Colored dots highlight localities discussed in the text. (For interpretation of the references to colour in this figure legend, the reader is referred to the web version of this article.)

often amplified by ecological regime shifts, lake ice-climate feedbacks or glacial flickering (Bakke et al., 2009; Brown and Duguay, 2010; Smol et al., 2005). An expanding method toolbox now allows us to fingerprint the depositional imprint of such changes at high resolution.

We present a sediment record spanning the past ~10 ka from the informally named Ymer Lake (65°37′N, 37°43′W), located on Ammassalik Island in southeast Greenland (Fig. 1). Its proximity to the Greenland Ice Sheet (GIS), the convergence of the polar East Greenland Current (EGC) and milder Atlantic Irminger Current (IC), the sea-ice limit as well as the oceanic polar front renders Ammassalik Island highly sensitive to regional climate change. This is evident from weather data as air temperatures in the island's main settlement, Tasiilaq, are rising by ~1.3 °C per decade (Cappelen et al., 2011), almost ten times the global average (IPCC, 2013). Straneo et al. (2010) show that the advection of subtropical surface waters into the adjacent Sermilik fjord compound on-going surface warming. Because of this powerful combination of rapid atmospheric and oceanic change, glacier retreat rates in the area rank amongst the highest on Greenland (Andresen et al., 2012; Bjørk et al., 2012).

The main goal of this study is to reconstruct the geomorphological expression of Holocene climate transitions on southeast Greenland and contextualize their causes. To do so, we seek to attribute depositional sediment signatures in Ymer Lake to specific surface processes. For this purpose, we employ a multi-proxy approach that combines multiple lines of visual, physical, magnetic and geochemical evidence (Bakke et al., 2010; van der Bilt et al., 2017). We expand this tested toolbox with Computed Tomography (CT) scanning, characterizing sediment structure in 3-D (Cnudde and Boone, 2013), and X-Ray Diffraction (XRD) analysis, fingerprinting sediment source area (Allen, 2008). We strengthen our proxy interpretations with the wealth of observational, modeling and geomorphological data available from Ammassalik Island. Finally, we integrate our findings in a regional paleoclimate framework.

2. Regional setting

Ymer Lake (65°37′N, 37°43′W) is located on Ammassalik Island, 100 km south of the Arctic Circle on the East Greenland coast (Fig. 1a–b). The open lake measures 0.29 km^2 and is fed by a 5.5 km^2 catchment. However, being part of a three-lake chain (Fig. 1c and 2a), a wider 30 km^2 watershed drains through Ymer Lake. To the North and South, alpine mountains flank the catchment and reach a maximum elevation of 916 m above sea level (m a.s.l) (Fig. 2a). The lake shorelines are mostly gentle sloping (0–5%) (Fig. 2b), buffering the basin from mass-wasting. Situated at 150 m a.s.l, Ymer lake lies above the reported 62 m a.s.l local Holocene marine limit (Humlum and Christiansen, 2008).

At present, a cirque glacier – here named Ymer Glacier - covers ~17% of the 5.5 km^2 catchment that directly drains into Ymer Lake (Fig. 2b). Documented past glacier positions demonstrate that Ymer glacier has been in retreat since at least 1930 (BAARE, 1930), in line with other glaciers on the island (Mernild et al., 2011). Beyond the instrumental era, an observation-constrained model proposes deglaciation of Ammassalik Island after 10 ka BP (Lecavalier et al., 2014). Subsequently, during the Holocene Thermal Maximum (HTM), warmer and drier conditions were unfavorable for glacier growth on East Greenland until 5 ka BP (Briner et al., 2016), prior to the onset of the Neoglacial period around 4 ka BP (Balascio et al., 2015). Fluted basal till and bedrock striations in the foreland of Ymer Glacier indicate a temperate (alpine) basal regime, as previously suggested by Humlum

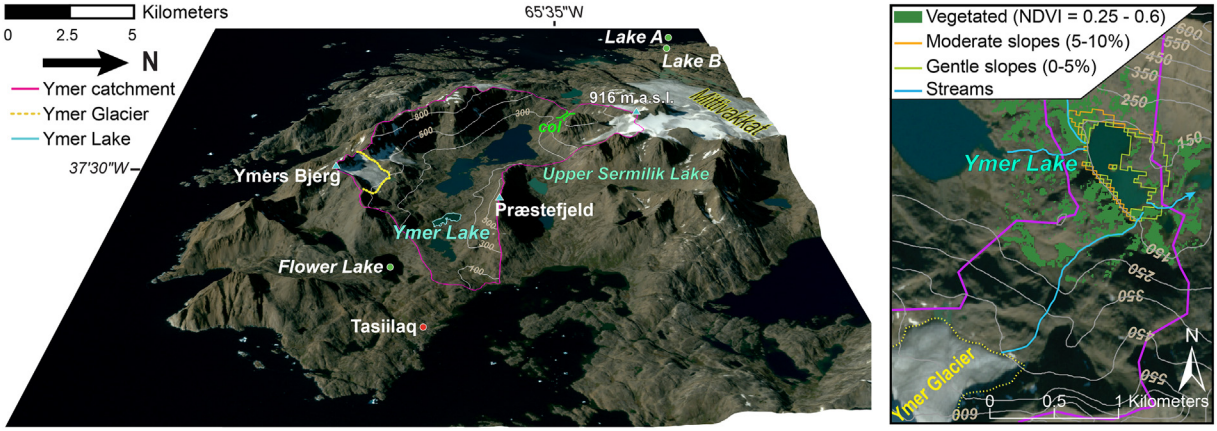

Fig. 2. A: a 3-D visualization of southern Ammassalik Island, draping a satellite image over a Digital Elevation Model (DEM) (ESA and EC, 2016; Howat et al., 2014). In addition to the outline (pink line) and 200 m contours (grey lines) of the wider Ymer watershed and the 2016 extent of Ymer glacier (dashed yellow line), topographical features and discussed sites are highlighted (colored dots). B: close-up of the catchment that directly drains into Ymer Lake, delimited by a purple line. Blue lines indicate streams, while 100 m contours are shown in grey. Vegetated sections of the catchment are highlighted by calculating the Normalized Difference Vegetation Index (NDVI) on satellite imagery. Gentle-moderate sloping sections bordering the lake shores are classified in orange and green from the DEM. (For interpretation of the references to colour in this figure legend, the reader is referred to the web version of this article.)

and Christiansen (2008). In addition to glacial melt water, a larger upstream lake and an ephemeral snow-fed stream on the lake's north shore feed Ymer Lake (Fig. 2b). Field mapping confirms that meltwater from the neighboring Mittivakkat glacier does not enter the Ymer watershed but drains into the adjacent Upper Sermilik Lake (Fig. 2a) (Davin, 2013).

Two bedrock formations underlay the Ymer catchment: 1) the Ammassalik Intrusive Complex (AIC), basic igneous rock with mainly orthopyroxene and intermediate plagioclase feldspar and local lenses of acidic diorite and 2) the Siportoq Supracrustal Association (SSA), metamorphosed sedimentary rocks that surround the AIC intrusion and predominantly consist of garnet-biotite gneisses (Fig. 1c) (Kalsbeek, 1989; Kolb, 2014). Whereas the intrusive AIC rocks envelop the shores of Ymer Lake and dominate the catchment, the SSA gneisses occur only near the catchment's southern limit (Fig. 1c). Notably, the cirque of Ymer glacier sits on the boundary between these mineralogically distinct formations. Bedrock exposures are most common in steep high parts of the catchment ($\geq$250 m a.s.l), particularly in the northeast.

In contrast, the lower lying ($\leq$250 m a.s.l) sections of the catchment are largely vegetated (Fig. 2b). Surficial sediment deposits are concentrated in the foreland of the Ymer Glacier and on the valley floor (Fig. 2a). Notable landforms include a glacio-fluvial outwash plain (Sandur) on the SE lake shores that is fed by Ymer Glacier (Fig. 3a), active dune fields ~1 km east of the lake (see also Humlum and Christiansen, 2008) as well as an incised gorge northwest of the lake that is over-dimensioned for the stream that runs through it today. In addition, talus mantles sections of the lower slopes of Præstefjeld Mountain (Fig. 2a).

Regional climate is strongly influenced by the interplay between the Irminger and East Greenland Currents (IC and EGC) (Fig. 1a) (Jennings et al., 2011). The former advects warm saline Atlantic water northwards and its volume transport is closely linked to the vigor of the Subpolar Gyre (SPG) (Fig. 1a) (Moffa-Sánchez et al., 2014). The latter exports cold fresh ice-laden waters southward from the High Arctic through the Fram Strait (Perner et al., 2016) (Fig. 1a). The dynamic interface between the IC and EGC determines the average position of the Arctic and Polar fronts, currently ~300 km north and south of our study site, respectively, across a steep Sea Surface Temperature (SST) gradient (Fig. 1a). Present-day climate on Ammassalik Island is low-Arctic maritime, with a mean air temperature of −4.5 °C and 870 mm of annual precipitation between 1895 and 2010 AD at Tasiilaq weather station (Cappelen et al., 2011; Klein Tank et al., 2002), 4 km SE of Ymer lake (Fig. 2a). Mernild et al. (2008) report that ~80% of precipitation falls as snow above 25 m a.s.l in the area. Wind direction and intensity also display a seasonal pattern: NE winds dominate year-round, but are strongest in winter (DJF). In contrast, SW winds are most common during summer (JJA) (Fig. 1c) (Gelaro et al., 2017), when the polar front lies north of the area.

3. Material and methods

3.1. Coring

Prior to coring, Ymer Lake was surveyed with a Garmin Fishfinder 160 sounder to generate a bathymetric map in Esri ArcMap 10.4. The lake comprises two basins separated by a shallow (1 m) sill (Fig. 3a): the deep (22 m) and steep Upper Ymer Lake (UYL) and shallow (5 m) gently sloping Lower Ymer Lake (LYL). Based on the bathymetry, we identified one coring location in each basin: deep, flat spots to minimize the risk of disturbance. Two piston cores were extracted: UYL-P1-14 (245cm) and LYL-P1-14 (228 cm). To warrant retrieval of surface sediments that overlap with observational time series, we also took gravity cores from the same locations: UYL-G1-14 (36 cm) from Upper Ymer Lake and LYL-G1-14 (36 cm) from Lower Ymer Lake. Distinct features can be correlated between the visual log and Magnetic Susceptibility (MS) stratigraphies of UYL-P1-14 and LYL-P1-14 (Fig. 3b), exhibiting a consistent cross-basin sediment signal. We nevertheless selected LYL-P1-14 as master core for this study: its greater distance from steep slopes and lake inlets renders the risk of sediment disturbance (e.g. mass wasting) lower (Figs. 2b & 3a).

3.2. Analyses

Following visual inspection, we measured surface Magnetic Susceptibility (MS) at 0.5 cm with a Bartington MS2E sensor on all extracted piston and gravity cores: primarily for the purpose of correlation (Fig.3b), but also to investigate links between minerogenic input and sediment provenance changes (Sandgren and Snowball, 2002). To determine fine-scale variations in minerogenic input, we mapped the geochemical composition of master core LYL-P1-14 with an X-Ray Fluorescence (XRF) scanner. A 200 µm resolution elemental profile was obtained with an ITRAX scanner fitted with a Chromium (Cr) tube set to 40 kV and 25 mA (n = 11,375). To characterize sediment structure in 3-D, core LYL-P1-14 was also scanned under a ProCon-X-Ray CT-ALPHA computed tomography (CT) scanner, set at 125 kV and 600 µA, creating 63.5 µm resolution 16 bit scans using a 267 msec. exposure time.

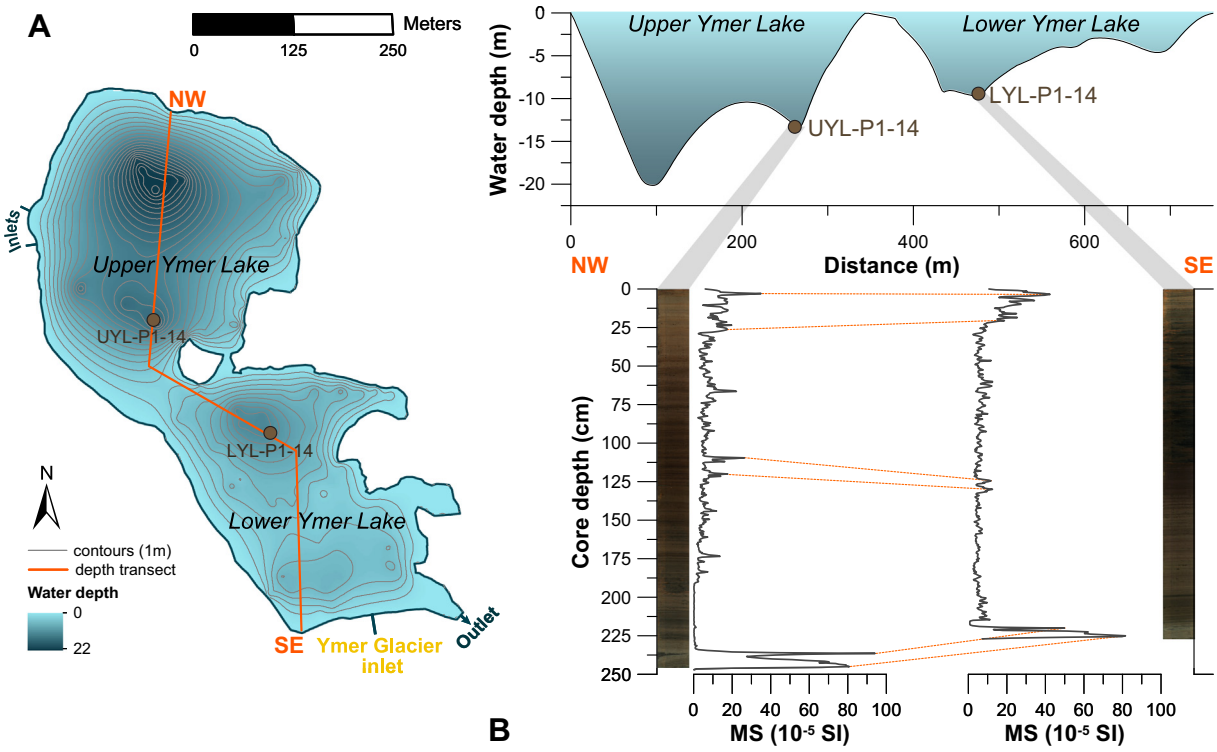

Fig. 3. A: Bathymetry of Ymer Lake with the locations of cores UYL-P1-14 and LYL-P1-14/LYL-G1–14, as well as the cross-lake transect shown in panel B. B: Northwest (NW) to Southeast (SE) transect through Ymer Lake through both coring locations. The bottom panel correlates distinct features in the Magnetic Susceptibility (MS) stratigraphy of the UYL-P1-14 and LYL-P1-14 cores.

Reconstructed scans were processed with the FEI Avizo 3D software suite, generating 752 × 9503 pixel 2-D slices (n = 405) and rendering a 0.24 mm^3 voxel volume (3-D).

We subsequently carried out a range of destructive analyses on master core LYL-P1-14 to further characterize the depositional signature of Ymer lake sediments. First, continuous 0.5 cm^3 cubes (n = 441) of sediment were extracted for weight Loss-On-Ignition (LOI) and Dry Bulk Density (DBD) measurements following the protocol by Dean Jr (1974). Next, 0.5 cm-thick slices were taken at 5 cm intervals (n = 41) for grain size analysis on a Malvern Mastersizer 3000 with a Hydro SV sampler. To remove organic particles prior to analysis, samples were treated with 95 °C aliquots of aqueous (35%) H_2O_2 until reaction ceased after Ryżak and Bieganowski (2011). We measured all grain size samples in fivefold to monitor analytical precision set by the ISO-13320 standard. Finally, to link lake sediment geochemistry and catchment bedrock mineralogy, we carried out qualitative X-Ray Diffraction (XRD) analysis on ± 0.5 cm^3 samples at 10 cm intervals (n = 20). Following the recommendations of Last and Smol (2002), we homogenized samples by sieving them through a 63 μm mesh and removing clay minerals using the gravity settling protocol outlined by Poppe et al. (2001). The resultant silt fraction was then measured as a randomly oriented dry powder, using a Bruker D8 ADVANCE ECO X-ray diffractometer, equipped with a 1.5418 Å Copper (Cu) source operated at 40 kV/25 mA.

3.3. Chronology

Thirteen plant macrofossil samples from core LYL-P1–14 were submitted for Accelerator Mass Spectrometer (AMS) radiocarbon dating (Table 1). To minimize chronological uncertainty (Oswald et al., 2005), we exclusively submitted *Betula* leaves. Following extraction, samples were send to the Poznan (Poz) radiocarbon laboratory for dating. To allow validation of proxy data against observational time series, the top 5 cm from gravity core LYL-G1-14 was sampled at 1 cm intervals for ^{210}Pb dating (n = 5). Following freeze-drying, ^{210}Pb activity was measured with an Ortec Alpha spectrometer at the Uranium-Series Dating Laboratory (USDL) of the University of Bergen.

3.4. Statistics

To support (visual) identification of lithostratigraphic core units, we carried out a constrained cluster analysis on a common 5 cm resolution (n = 43) on all measured proxy variables: 16 sensitively measured XRF elements (Coxsys, 2006), grain size distribution data, LOI, DBD as well as MS measurements. Prior to analysis, included variables were standardized and transformed into compositional data. For this purpose, we employed the 0.9–9 Rioja package by Juggins (2009) in version 3.4 of the R environment (RCoreTeam, 2014), expressing dissimilarity as Euclidean distance. To identify the number of significant units, we ran a broken stick model with the default settings of the 0.9–9 Rioja package. Raw XRF measurements were integrated at 0.5 cm intervals to smooth out noise using the regular interpolation algorithm in Past 3 at 0.5 cm (Hammer, 2013). The GRADISTAT program by Blott and Pye (2001) was used to calculate metric Folk and Ward measures for all grain size distribution data.

4. Results

4.1. Sedimentary properties

A broken stick model (see Section 3.4) identified four significant clusters in master core LYL-P1-14 (see Section 3.4). We used these findings to complement information gained by visual inspection (logging) to subdivide the record in four lithological units: 4 (228–218 cm), 3 (218–130 cm), 2 (130–35 cm) and 1 (35–0 cm), from bottom to top. We characterize these sections with a multi-proxy approach by presenting continuous down-core variations in 1) colour and structure, 2) sediment organic content (LOI) - detecting shifts in biological

Table 1
Overview of radiocarbon samples extracted from core LYL-P1-14.

Core	Lab nr.	Material	Sample weight (mg)	Depth (cm)	^{14}C (BP)	Min. age (cal BP)	Max. age (cal BP)	Fit (cal BP)
LYL-P1	Poz-72,583	Betula leaves	26.6	2	80 ± 30	−22	−4	−13
LYL-P1	Poz-72,584	Betula leaves	47.1	25	865 ± 30	531	880	713
LYL-P1	Poz-72,585	Betula leaves	44.5	41	1350 ± 35	1036	1323	1202
LYL-P1	Poz-72,586	Betula leaves	37.5	53	1715 ± 30	1442	1685	1561
LYL-P1	Poz-72,725	Betula leaves	44.4	71	2470 ± 30	2126	2672	2414
LYL-P1	Poz-72,726	Betula leaves	32.3	110	3760 ± 35	3647	4320	4034
LYL-P1	Poz-72,629	Betula leaves	51.7	116	4065 ± 30	4193	4525	4346
LYL-P1	Poz-71,712	Betula leaves	50.9	146	5310 ± 40	5590	6222	5962
LYL-P1	Poz-72,768	Betula leaves	12	167	5860 ± 40	6451	6829	6648
LYL-P1	Poz-72,630	Betula leaves	18.1	195	6800 ± 40	7255	7801	7569
LYL-P1	Poz-75,498	Betula leaves	6 (0.8 mg C)	212	8480 ± 40	7974	9491	8936
LYL-P1	Poz-72,632	Betula leaves	5.4	218	2225 ± 30	–	–	–
LYL-P1	Poz-75,499	Betula leaves	2.1 (0.08 mg C)	219	6330 ± 70	–	–	–

productivity or preservation (Last and Smol, 2002), 3) density (DBD) - tracking variations in bulk minerogenic input (Bakke et al., 2005), 4) Magnetic Susceptibility (MS) - reflecting catchment-derived input (Sandgren and Snowball, 2002), 5) grain size distribution - fingerprinting the signature of minerogenic sedimentation (Vasskog et al., 2011), and 6) elemental concentrations (XRF) - capturing shifts in lake geochemistry or the source of minerogenic input (Davies et al., 2015). From the measured XRF elements, we use Calcium (Ca) to track shifts in the source of minerogenic input for two reasons. Firstly, Ca is a major component of the intermediate plagioclase feldspar that dominate the AIC bedrock surrounding Ymer Lake (Fig. 1c) (Kolb, 2014). Secondly, Ca is highly sensitive to the Cr tube used for XRF measurements (Coxsys, 2006). We also normalize mobile Iron (Fe) against conservative Titanium (Ti), a widely used ratio to detect changes in redox diagenesis (Croudace et al., 2006) (Section 5.3). To further link sediment geochemistry and bedrock mineralogy, we complement XRF data with XRD measurements from selected intervals (Fig. 5). Finally, we present 2-D and 3-D CT imagery to visualize the relationship between down-core proxy changes and sedimentary structures after e.g. Fouinat et al. (2017) (Fig. 6).

4.1.1. Unit 4 (228–218 cm)

Unit 4 covers the lowermost 16 cm of core LYL-P1–14 and comprises packed grey-brown silts (Fig. 4). The highest DBD (~ 3 g cm^3), MS (~ 60*10–5 SI) and Ca (~ 2500 cps) values of the entire record (Fig. 4) highlight the dense minerogenic character of the sediments. Underlining the robustness of this relationship, multivariate linear regression of MS and DBD on Ca yields an adjusted R_2 value of 0.70 ($p < .05$, $n = 15$). The XRD patterns of Fig. 5 shows that unit 4 contains both intermediate plagioclase feldspar, as well as biotite-group minerals. Although the sediments exhibit no clear visible structures, CT imagery reveals the presence of irregular mm-scale laminations (Fig. 6a). Tapering of laminae towards the tube edge is a coring artifact. The boundary with overlying unit 3 around 9 cal. ka BP is sharp and marked by a distinct ± 1 cm lens (Figs. 4 and 6a), predominantly consisting of sand (Figs. 4 and 6a), which is also found in sediments from Upper Ymer Lake (Fig. 3b). Owing to this coarse texture, grain size could not be measured with the Mastersizer 3000 (see Section 3.2) and had to be determined with a comparator, instead. We use this clastic layer as a reference for the CT greyscale density values of purely minerogenic sediments in Ymer Lake, rendering this range (2850–4500) pink in Fig. 6a. The high-resolution CT ortho slice of Fig. 6a also shows that the laminae that border this lens are comparatively thick.

4.1.2. Unit 3 (218–130 cm)

Minerogenic indicators DBD, MS and Ca rapidly decline across the transition into unit 3 (Fig. 4). In contrast, organic content, reflected by LOI percentages, exhibit a steep concomitant rise. While prompt, the transition from unit 4 at 218 cm isn't marked by a truncated erosive boundary (Fig. 6c). Unit 3 sediments are regularly (~0.5 cm) laminated throughout and shift in colour from grey-brown to dark brown towards the top (Fig. 3b). As shown in Fig. 4, this gradual transition corresponds to a decrease in minerogenic content, reflected by attenuating DBD and Ca values. As in unit 4, fine sediments dominate the grain size signature of minerogenic input. XRD analysis highlights differences in the mineralogical signature between the two units: biotite-group minerals are almost absent in unit 3 (Fig. 5).

4.1.3. Unit 2 (130–35 cm)

Generally, unit 2 comprises a dark brown gyttja that displays faint mm-scale laminae (Fig. 3). While visually homogeneous, the lowermost 20 cm of unit 2 mark a shift in depositional conditions in Ymer Lake as organic content and redox-sensitive Fe/Ti rapidly rise from ~5000 cal. yr BP (Fig. 4). While minerogenic sediment content is minimal throughout unit 2, as demonstrated by low and stable DBD, MS and Ca values, the most abundant grain size fraction of clastic input changes sharply from silt- to sand-sized particles after ~4.2 cal. ka BP (Fig. 4). This coarsening characterizes unit 2 sediments, but closer inspection reveals distinct intervals consisting of finer grained (coarse silt) clastic input. CT imagery of the most distinct of these horizons (Figs. 4 and 6b), which again highlights clastic input by selecting the grey-scale range of rendered minerogenic unit 4 sediments (Fig. 6b), reveals mm-scale lamination. Towards the boundary with unit 1 at 35 cm depth, sediment grain size again changes, shifting to a mode and range that is similar to the minerogenic silts of unit 4 (Fig. 4).

4.1.4. Unit 1 (35–0 cm)

Unit 1 represents the first period of predominantly minerogenic sedimentation in Ymer Lake since deposition of unit 4 (Fig. 4). The grain size signature of measured samples shifts at the boundary with unit 1: silt replaces sand as the modal particle size after ~1.2 cal. ka BP. CT imagery highlights this rapid transition: as before, we highlight clastic material using the grey-scale range of unit 4 sediments as a reference. Fig. 6c reveals the rapid rise of finer minerogenic input across the boundary from unit 2. This trend is reflected in finer detail by the concurrent rise in DBD, MS and Ca, reaching values not recorded since unit 4 (Fig. 4). Multivariate linear regression of MS and DBD on Ca yields an adjusted R_2 value of 0.76 ($p < 0.05$, $n = 60$), showing that these minerogenic indicators increase concomitantly. XRD analysis reveals that the mineralogy of unit 1 resembles that of unit 4 as the sediments contains phases of biotite minerals (Fig. 5).

4.2. Age-depth model

We generated an age-depth model for master core LYL-P1–14 using the Bacon 2.2 package by Blaauw and Christen (2011), run in version 3.4 of the R environment (RCoreTeam, 2014). Ages were modeled at 0.5 cm intervals, using a 20 yr/cm accumulation rate and default

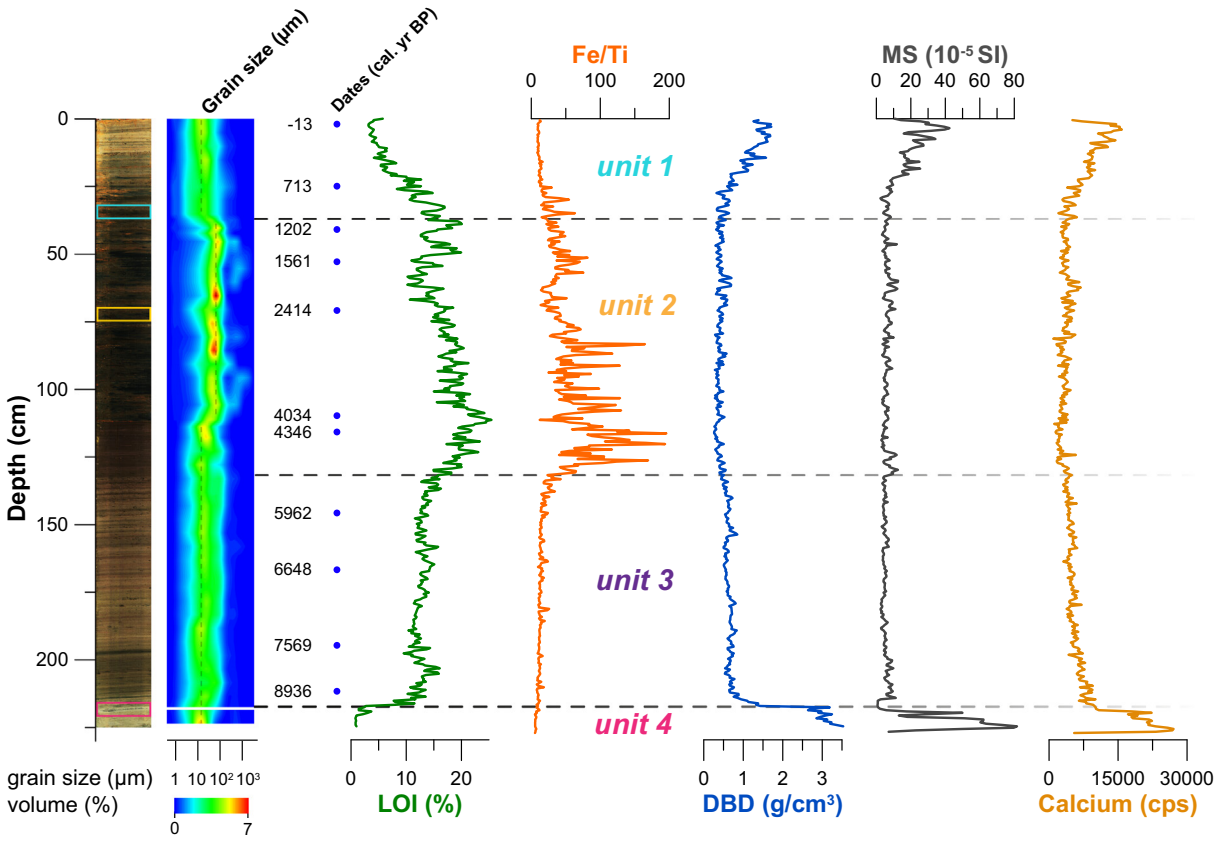

Fig. 4. Down-core measurements of grain size distribution (surface plot), physical indicators LOI and DBD, elemental proxies Fe/Ti and Calcium (Ca) and magnetic indicator MS on LYL-P1–14. Note: the 218–219 cm interval is left empty in the surface plot because clasts were too large for Mastersizer analysis (see paragraph 3). Also shown is a core image (far left) as well as calibrated ^{14}C ages (blue dots). Colored rectangles highlight the down-core locations of the CT scan insets shown in Fig. 6. Dashed horizontal lines mark unit boundaries. (For interpretation of the references to colour in this figure legend, the reader is referred to the web version of this article.)

memory parameters as priors, while using the IntCal13 curve for calibration (Reimer et al., 2013). All ^{14}C ages (n = 13) were included in the model (Fig. 7a), highlighting small and improbably young (inverted) samples Poz-72,632 and Poz-75,499 as likely outliers (Table 1). ^{210}Pb ages were not calibrated in Bacon, but calculated from ^{210}Pb activity measurements on surface core LYL-G1–14 (n = 5) using the CRS model by Appleby and Oldfield (1978). This chronology was then transferred to the depth-scale of LYL-P1–14 by correlating respective MS stratigraphies in the Analyseries 1.2 software package (Fig. 7b) (Paillard et al., 1996).

5. Discussion

5.1. Deglaciation, local glacier retreat and lake outburst flooding (10–9.5 cal. ka BP)

Basal unit 4 (228–218 cm) is characterized by fine-grained (silty) highly minerogenic sediments, as previously outlined, and summarized in Figs. 8e and f. The mm-scale observed laminae suggest accumulation in a low-energy environment. Following e.g. and Peach and Perrie (1975), we attribute this distinct sediment signature to the deposition of rock flour. This fine-grained product of glacial erosion is easily suspended in meltwater streams and may be trapped in tranquil downstream lakes (Karlén, 1976; van der Bilt et al., 2016). Our interpretation is supported by the strong correspondence between unit 4 and contemporary unit 1 sediments (Figs. 4, 8e and f), deposited during a period of documented glacier activity in the catchment (see Section 2). The XRD data support this as units 4 as well as 1 contain Biotite phases (Fig. 5). Although both rock formations in the catchment area contain biotite, it is only a major component in the garnet-biotite gneisses of the Siportoq Supracrustal Association (SSA). The clear presence of biotite in this unit thus suggests that these sediments (partially) derive from SSA bedrock, and that glacier coverage during deposition of unit 4 occupied the southeastern part of the catchment. The current presence of a glacier in this area of the catchment, and the correspondence between sediments from unit 4 and the contemporary unit 1 sediments, supports this interpretation. The presence of biotite may also explain the comparatively high MS values of unit 4 sediments as micas are strongly (para)magnetic (Rosenblum and Brownfield, 2000). In conclusion, we claim that, like today, up-stream erosive (alpine) glaciers fed Ymer Lake between ~10,000–9600 cal. yr BP. This requires that the Greenland Ice Sheet (GIS) or other remnant ice had vacated the Ymer Lake basin prior to the onset of lacustrine sedimentation ~10,000 cal. yr BP. As shown in Fig. 8i, this estimate for the deglaciation of Ammassalik island is consistent with modeling evidence from Lecavalier et al. (2014) (Fig. 1b), cosmogenic ages of glacially abraded bedrock in nearby Torqulertivit Imiat valley (Fig. 1c) (Roberts et al., 2008), as well as ^{14}C-dated isolation basins on the adjacent Qernertivartivit island (Fig. 1c) (Long et al., 2008).

In keeping with the above interpretation, we argue that the sharp decline in minerogenic input across the transition into unit 3 around 9600–9500 cal. yr BP marks the disappearance of glaciers from the Ymer catchment (Fig. 8f). As shown in Figs. 8c and h, respectively, this period coincides with 1) the onset of a Sea Surface Temperature (SST) optimum in the Kangerlussuaq trough of the adjoining southern Denmark Strait (Fig. 1b) (Andersen et al., 2004), 2) a Holocene maximum in Chironomid-derived summer temperatures near Scoresby Sund on the central East Greenland coast (Figs. 1a and 8c) (Axford et al., 2017)

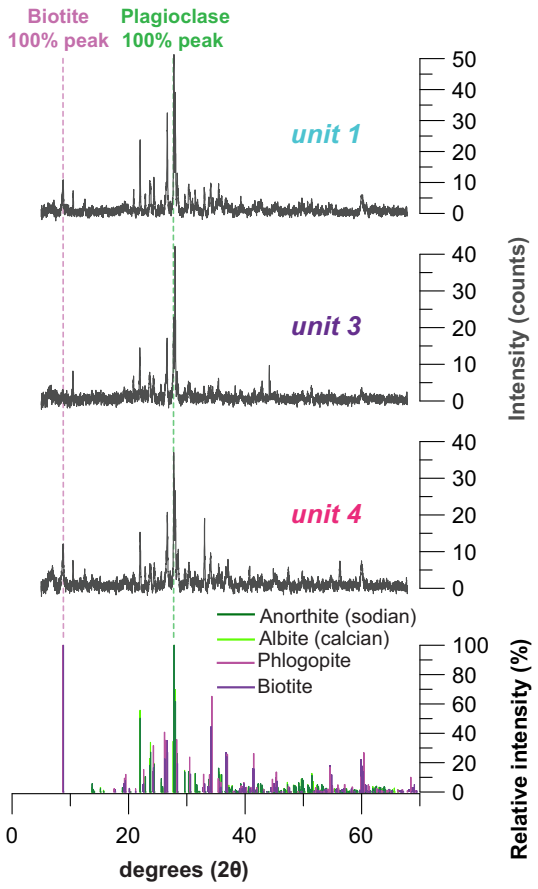

Fig. 5. XRD diffractograms of samples from units 4, 3 and 1, compared to reference stick patterns and 100% (most diagnostic) peaks of biotite (biotite and phlogopite) and intermediate plagioclase (sodian anorthite and calcian albite) group minerals derived from the ICCD (2007) database. We could not measure unit 2 by XRD due to high organic sediment content, obscuring diffraction maxima.

and 3) rapid GIS mass loss at the ice-core site closest to our study area, Dye-3 (Figs. 1b and 8i) (Lecavalier et al., 2014). In light of the above, we attribute glacier loss in the Ymer catchment ~9600–9500 cal. yr BP to rising regional surface temperatures.

The outlined interplay of forcing mechanisms, set against the backdrop of a summer insolation maximum (Huybers, 2006), may also help explain the sandy lens that caps unit 4 (Fig. 6a). Its coarse grain size signature indicates transport under high-energy conditions, while the sharp compositional contrast with sediments accumulated before and after suggests deposition during an abrupt extreme event. As observed at present (Zhang et al., 2015), moraine- or ice-dammed proglacial lakes rapidly form and expand during periods of glacial retreat (Carrivick et al., 2013). When breached, the subsequent high-energy Glacial Lake Outburst Flood (GLOF) flushes available coarse-grained sediments into downstream lakes while finer sediments remain suspended in the torrent. Integrating observations and sediment cores from a glacier-fed lake in Norway, Xu et al. (2015) show that fingerprinted distal lacustrine GLOF deposits have a similar thickness (~1 cm) and modal grain size (coarse sand) as well as sharp boundaries and thicker-than-normal adjoining fine-grained laminae as the lens capping unit 4. Speculating about the pattern of damming, any up-stream impoundment has the potential to pond water before spilling through the lowest col in the NW of the watershed (Fig. 2a). The ensuing pattern of meltwater discharge may also explain formation of the over-dimensioned incised gorge NE of Ymer Lake (see Section 2). In conclusion, we argue that deglaciation of the catchment ended catastrophically: rapid

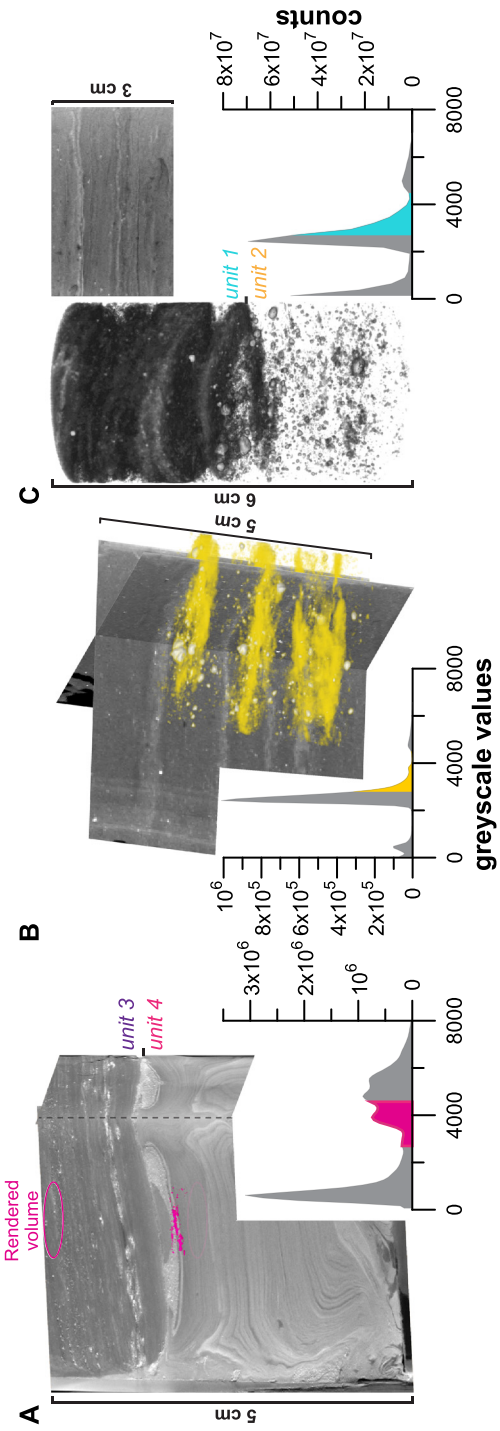

Fig. 6. CT scan (ortho) slices with highlighted greyscale values in histograms of A: the transition between units 3 and 4, including a volume rendering of the sandy deposit that caps unit 4, B: a volume-rendered event layer in unit 2 between 70 and 75 cm core depth and C: the transition between units 1 and 2. Note: Fig. 4 highlights the depth intervals of all CT slices with corresponding colors.

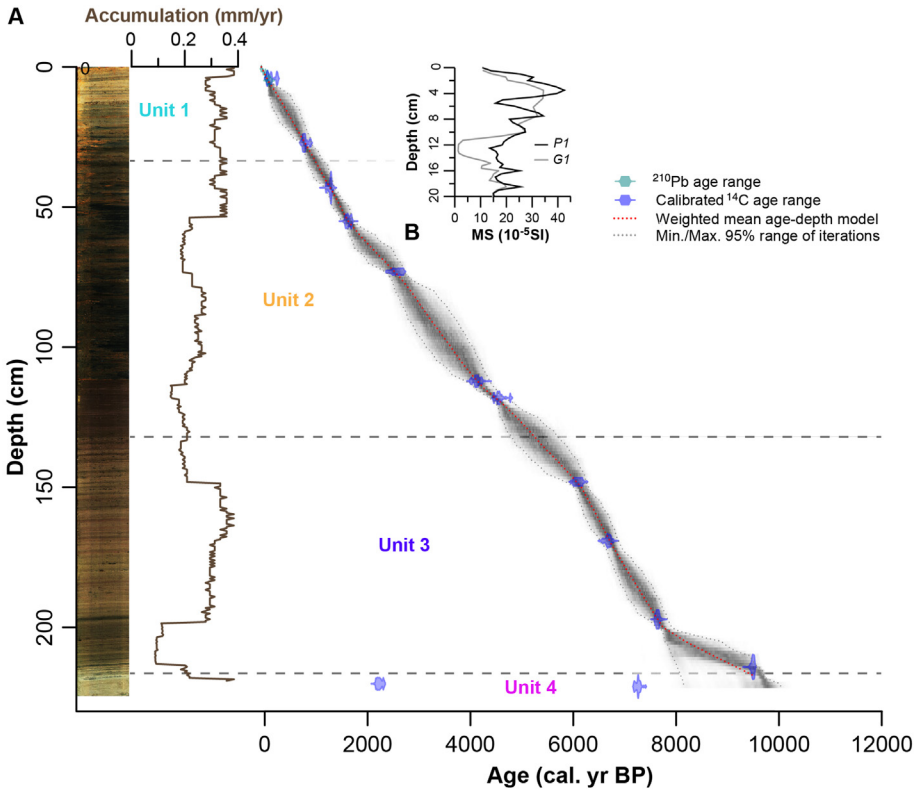

Fig. 7. A: Age-depth relation generated for core LYL-P1–14, plotting interpolated accumulation rates, and showing the weighted mean as well as 95% confidence limits, in addition to the calibrated ranges of radiocarbon ages in blue. A core image is shown on the far left and dashed lines mark unit boundaries. B: Inset of the overlapping MS stratigraphies of cores LYL-P1–14 and LYL-G1–14. (For interpretation of the references to colour in this figure legend, the reader is referred to the web version of this article.)

regional warming drove the formation and collapse of an upstream ice-marginal lake, releasing an outburst flood into Ymer lake.

Finally, we note that the reported timing of local glacier disappearance from the nearby Flower and Kulusuk lake catchments (Figs. 1c, 2a, 8g and i) (Balascio et al., 2015; Balascio et al., 2013), characterized by a similar elevation gradient (hypsometry), post-date our findings by more than a millennium - 8.4 and 7.8 cal. ka BP, respectively. While age-depth model uncertainties provide a likely explanation (Fig. 6), this incongruity could also signify a heterogeneous response of Ammassalik island's glaciers.

5.2. Quiescent Holocene optimum shaped by glacial or wind-blown clastic background sedimentation (9.5–5 cal. ka BP)

The Early Holocene sediments of unit 3 (218–130 cm) mark a quiescent phase in the evolution of Ymer Lake between 9.5 and ~ 5 cal. ka BP. As shown in Figs. 4, 8e and f, minerogenic content, mean grain size and redox-sensitive Fe/Ti vary little towards the Mid-Late Holocene transition. Together with the persistence of regular lamination (Fig. 6a), this evidence suggests stable depositional conditions. Also, after the cessation of glacial input ~9500 cal. yr BP, minerogenic sediment content remains low (Fig. 8f). Coincidence with the Holocene Thermal Maximum (HTM) on East Greenland likely compounded this shift (Fig. 8c) (Axford et al., 2017; Briner et al., 2016), enhancing lake productivity and diluting clastic input with organic matter (Rollison, 1993). Closer inspection demonstrates that the minerogenic content of Ymer lake sediments continues to diminish into unit 3, only falling below average (z = 0) values between ~7500–7000 cal. yr BP (Fig. 8f). Balascio et al. (2013) provide an explanation for this gentle decline, inferring a phase of post-glacial stabilization in the adjacent Flower Lake catchment until ~7 ka BP (Fig. 2a), based on diatom analysis.

While the above suggests that the Early Holocene in Ymer Lake is defined by an attenuation of minerogenic sedimentation, our XRD data indicate that provenance of clastic input also shifts from unit 4 to 3 (Fig. 5). The dominance of intermediate plagioclase and absence of biotite suggests that basic igneous AIC bedrock dominates the source of minerogenic material in unit 3 (Fig. 1c). Given that clastic sedimentation continues to be silt-dominated as in (de)glacial unit 4 (Fig. 8e), we propose two potential sources.

Firstly, unit 3 sediments may comprise glacial flour from a body of ice in the northwest sector of the wider Ymer watershed. As the highest part of southern Ammassalik (Fig.2a), with a maximum elevation of 1084 m a.s.l (against 809 m a.s.l in the Ymer catchment), the NW is the likeliest area for glacial ice to have persisted into the HTM. Indeed, at present, it is the most glaciated part of the island, covered by the Mittivakkat glacier. In addition, and unlike the highest parts of the Ymer catchment, bedrock in this area consists mainly of the orthopyroxene and intermediate plagioclase-rich rocks of the AIC, consistent with the mineralogical signature of unit 3 sediments (Fig. 1c). Moreover, explaining the weakness of the discussed fine-grained minerogenic signal in Ymer Lake, any up-stream glacier first drained into the larger upstream lake (Fig. 2a); as shown by Liermann et al. (2012), the most ice-proximal glacier-fed lakes trap 80–85% of suspended rock flour. However, with inferred regional summer air temperatures of up to ~3 °C above preindustrial values (Axford et al., 2017; Dahl-Jensen et al., 1998)(Fig. 8c), it may have been too warm to sustain glaciers. Modeling evidence suggests that, even under cooler present-day conditions, up to 80% of the volume of Mittivakkat glacier will melt (Mernild et al., 2011). Moreover, a compilation of hydroclimate reconstructions shows that East Greenland was also drier during the Early Holocene (until ~5 ka BP) (Briner et al., 2016), further hindering ice accumulation. Finally, as the Mittivakkat glacier feeds an adjacent watershed (Section 2), Early Holocene glacial meltwater input into Ymer Lake requires a different drainage network or ice configuration.

Alternatively, we hypothesize that aeolian processes may have deposited the silty plagioclase-dominated clastic sediments of unit 3. Following deglaciation, fine-grained glacigenic material would have been readily available for modification on fresh forelands in the Ymer catchment. As highlighted by Ballantyne (2002), such settings are highly susceptible to paraglacial re-deposition of fine sediments. Contemporaneous climatic conditions likely enhanced this sensitivity, because wind erosion is more effective under the dry conditions that

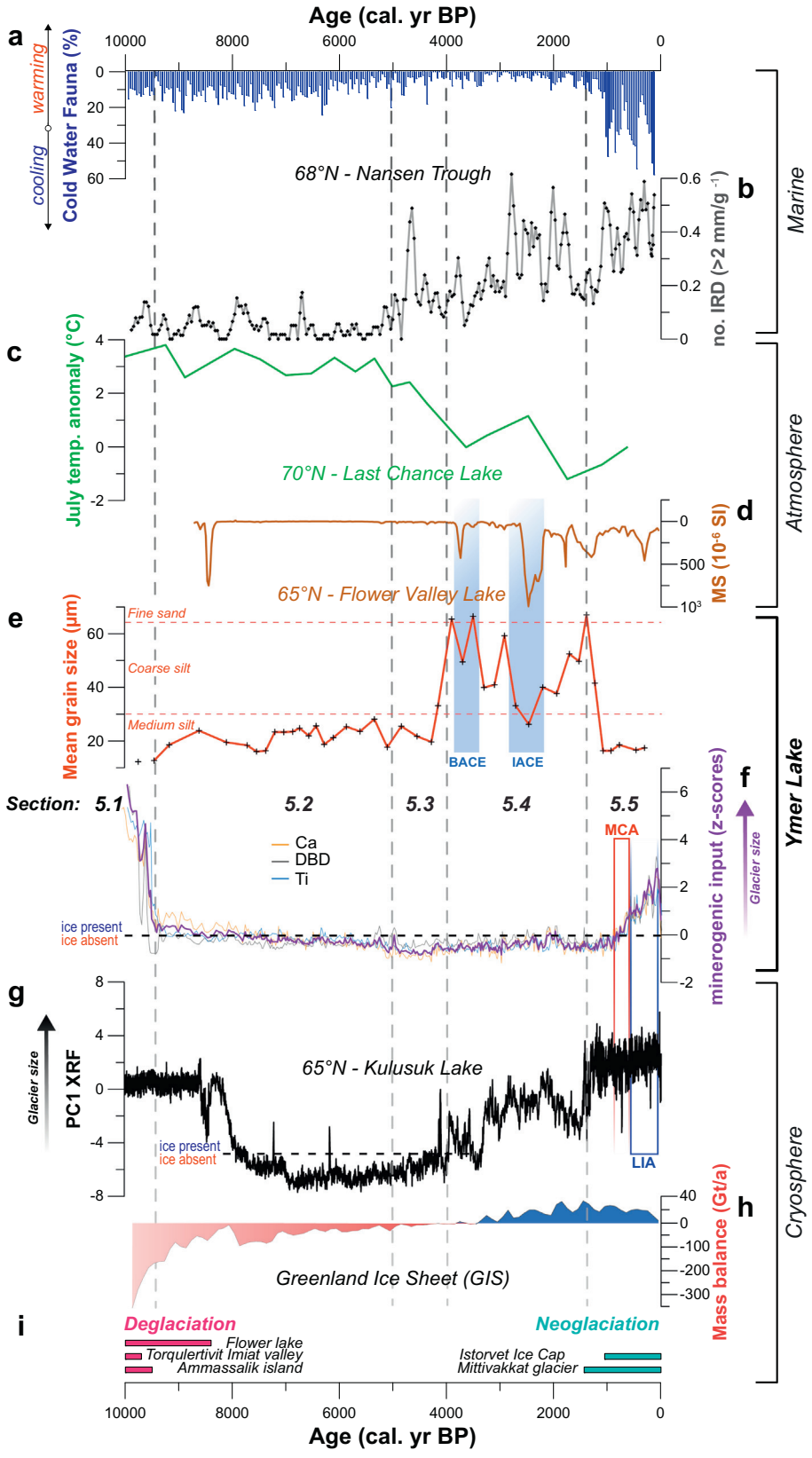

Fig. 8. Comparison of key Ymer Lake proxies, E: mean grain size variability (µm) and F: standardized values of minerogenic (glacigenic) indicators DBD, Ca and MS with a compilation of regional reconstructions of Holocene oceanic, atmospheric and cryospheric change. A: cold water planktonic foraminifera fauna abundance (%) in the Nansen Trough (Fig. 1b) (Perner et al., 2016). B: Counts (mm/g^{-1}) of IRD (> 2 mm) in Nansen Trough sediments (Perner et al., 2016). C: Chironomid-based calibrated (FOR-15) terrestrial summer (July) temperatures from Last Chance Lake in the Scoresby area (Fig. 1b)(Axford et al., 2017). D: MS-based flood reconstruction of run-off events from Flower Lake on Ammassalik island (Fig. 2a) (Balascio et al., 2013). G: XRF-based PC1 glacier activity reconstruction of Kulusuk glacier (Balascio et al., 2015). H: Holocene Greenland Ice Sheet (GIS) mass balance (Gt/a) at Dye3 (Fig. 2b), reconstructed with the Huy3 model by Lecavalier et al. (2014). I: Bars indicating the dated onset of deglaciation (pink) and Neoglaciation (blue) in our study area. Sources: Flower lake (Fig. 2) - ^{14}C-dated lake sediments (Balascio et al., 2013), Torqulertivit Imiat (Fig. 1c) - ^{10}Be exposure ages (Roberts et al., 2008), Ammassalik island (Fig. 1c) - ^{14}C-dated isolation contacts (Long et al., 2008), Istorvet Ice Cap (Fig. 1a) - ^{14}C-dated lake sediments (Miller et al., 2013), as well as Mittivakkat glacier (Fig. 2a) - ^{14}C-dated plant macrofossils (Hasholt, 2000). (For interpretation of the references to colour in this figure legend, the reader is referred to the web version of this article.)

prevailed on East Greenland during the Early Holocene (Benn and Evans, 2014; Briner et al., 2016). Indeed, Christiansen et al. (1999) date the onset of aeolian-dominated sedimentation on the western sector of Ammassalik Island around 6500 ± 700 cal. Yr BP, based on a luminescence-dated (OSL) profile. However, this "paraglacial" scenario does not explain the biotite-free mineralogy of unit 3, as it is reasonable to assume that the (de)glacial sediments in the Ymer catchment comprise a mixture of biotite-rich (SSA) and biotite-poor (AIC) bedrock types (see Section 5.1). The modern geomorphic setting of the catchment may provide a more apt analogue (see Section 2), since active dunes occupy

the south slopes of Præstefjeld Mountain, ~1 km east of Ymer Lake (Fig. 2a). Critically, Humlum and Christiansen (2008) assert that these are sourced from the immediate surroundings, which are exclusively underlain by the plagioclase-dominated AIC rocks that characterize the mineralogy of unit 3 (Figs. 1c and 7). While these present-day dunes consist of a coarser grain size fraction (sand) than unit 3 sediments, Early Holocene dunes could have been located further from Ymer Lake. Reviewing field evidence, DeVries-Zimmerman et al. (2014) assert that dune sand particles can only be suspended for a maximum of 200 m.

In summary, we argue that either glacier-derived or wind-blown clastic material dominated Early Holocene minerogenic background sedimentation in Ymer Lake. While the fine grain size signature of the sediments support the former scenario, coeval warm and dry conditions as well as a homogeneous sample mineralogy favor a (local) aeolian origin.

5.3. Lengthening lake ice coverage, shifting wind patterns and increased avalanching at the start of the Neoglacial (5–4 cal. ka BP)

The transition into the Late Holocene is marked by two marked changes in Ymer Lake. LOI and Fe/Ti rise in tandem from ~5 cal. ka BP (~130 cm) (Fig. 4), indicating more reducing conditions (Croudace et al., 2006; Cuven et al., 2010). As outlined by e.g. Anthony (1977), soluble Fe (II) accumulates in the water column during anoxic conditions. When the water column subsequently mixes following e.g. lake ice melt, built-up Fe oxidizes and precipitates as insoluble Fe (III) oxides. After 4.2 cal. ka BP, the mean grain size of Ymer lake sediments shifts from silt- to sand-dominated clasts (~113 cm) (Fig. 8e).

Other proxy records from Ammassalik Island reveal contemporaneous shifts and contextualize our findings from Ymer Lake with independent lines of evidence. Balascio et al. (2013) infer a lengthening of seasonal ice coverage on neighboring Flower Lake (Fig. 2a), based on the progressive depletion of leaf wax δD values from 5 to 4.1 cal. ka BP. Jakobsen et al. (2008) draw a similar conclusion for lakes A and B on the northwestern part of the island (Fig. 2a), based on abrupt paleoecological changes around ~4.5 cal. ka BP. As reported by e.g. Cuven et al. (2010), extended ice coverage prevents mixing of the water column, depleting bottom (hypolimnion) oxygen concentrations. Ensuing redox-related diagenesis could account for the concomitant increase in Fe/Ti and LOI values in Ymer lake sediments as anoxic-hypoxic conditions restrict the degradation of organic matter while (re) mobilizing iron (Fe). Such climate-lake ice feedbacks are typical for shallow high-latitude sites like the lower basin of Ymer Lake (Brown and Duguay, 2010).

This scenario can also help explain the reported coarsening of clastic input around 4.2 cal. ka BP (Fig. 8e). Ice provides a solid surface for the transportation of coarser clasts onto lakes (Luckman, 1975), enabling deposition in central parts like our coring location (Fig. 3a). Lengthening of seasonal ice coverage on Ymer Lake would have maintained this sediment pathway into the avalanche-prone spring season. Christiansen et al. (1999) also report activation of avalanche/nivation slopes on Ammassalik Island during this time (3900 ± 600 cal. yr BP), enhancing contemporaneous fluxes of coarser clasts towards Ymer Lake. Indeed, the coarse, sandy composition of unit 2 is diagnostic for niveo-aeolian deposits in other Arctic lakes (Lamoureux and Gilbert, 2004b).

We postulate that longer seasonal ice coverage and increasing avalanching prompted clastic coarsening and redox diagenesis (indicated by higher and co-varying LOI and Fe/Ti values) of Ymer lake sediments across the Middle-Late Holocene boundary.

Comparison with other paleoclimate records from East Greenland demonstrates that these changes mark a local response to regional climate deterioration at the onset of the Neoglacial period; a cooling response to declining Northern Hemisphere summer insolation (Wanner et al., 2011). Collating lake records from (south)east Greenland, Briner et al. (2016) presents evidence for widespread terrestrial cooling after ~5 cal. ka BP. This is corroborated by the quantitative Chironomid-derived July air temperature reconstruction from Scoresby Sund by Axford et al. (2017) (Figs. 1b and 8c). Documenting the response of the cryosphere to Neoglacial cooling, Balascio et al. (2015) infer glacier re-growth on nearby Kulusuk island after 4.1 cal. ka BP (Figs. 1c and 8g). Also, the GIS concurrently tipped into positive mass balance at the ice core site closest to Ymer Lake, Dye-3 (Figs. 1b and 8h) (Lecavalier et al., 2014). Demonstrating that climate deterioration extended beyond the terrestrial realm, Perner et al. (2016) reconstruct a coeval increase in Ice Rafted Debris (IRD) in the northern Denmark Strait (Figs. 1b and 8b), indicative of a strengthening East Greenland Current (EGC). Using foraminiferal evidence, Andresen et al. (2013) infer cooling in Sermilik Trough after 4.2 cal. ka BP (Fig. 1c), showing that Neoglacial cooling also influenced the coastal waters of Ammassalik Island.

Jennings et al. (2011) present a compelling process-based framework that reconciles the coincidence of regional Neoglacial cooling with longer seasonal lake ice coverage and increased avalanching in the Ymer catchment, invoking shifting wind patterns. As the GIS advanced and the EGC strengthened, higher atmospheric pressure and an advancing oceanic Polar Front (Fig. 1a) increased the frequency of northerly winds. Both geomorphological observations and instrumental data support this scenario. Christiansen et al. (1999) indicate that Neoglacial activation of snow avalanching on Ammassalik Island was restricted to SW-facing slopes, suggesting that dominant winds indeed shifted to the North (NE). Providing a modern analogue for this shift, Oltmanns et al. (2014) demonstrate that NE winds are more frequent on Ammassalik island under colder conditions. Bearing in mind that the steepest slope in the Ymer catchment, flanking Præstefjeld mountain, is SW facing (Figs. 2a and b), local conditions are particularly conducive to snow avalanching under a NE-dominated wind regime. A shift in prevalent wind direction may also reconcile the offset between Late Holocene re-growth of the Kulusuk (~4.1 ka cal. BP) and Ymer (~1.2 ka cal. BP) glaciers (Fig. 8) (Balascio et al., 2015). While of a similar size and sitting at the same altitude, Ymer glacier faces windward (NE) whereas Kulusuk glacier faces leeward (SW) - capturing wind-drifted snow under a NE-dominated wind regime. Hasholt et al. (2003) show that this process affects glacier mass balance on Ammassalik Island by redistributing ~10% of precipitation.

5.4. Snow-melt driven flooding during the Bronze Age and Iron Age cold epochs (4–1.2 cal. ka BP)

Generally, clastic input into Ymer Lake remains comparatively coarse from ~4 cal. ka BP until the transition into unit 1–35 cm depth (~1.2 cal. ka BP). However, CT imagery and grain size distribution highlight finer-grained minerogenic intervals with a single mode in the coarse silt fraction (Figs. 8e and 5e). In keeping with Vasskog et al. (2011), we attribute this distinct signature to flooding. Concurrence of these intervals with a MS-inferred runoff event from neighboring Flower Lake by Balascio et al. (2013) supports this interpretation. By integrating photographic time lapses and stream discharge data, Mernild and Hasholt (2006) reveal that runoff on Ammassalik island peaks during the snow melt period, providing a possible modern analogue for Late Holocene flooding. Moreover, using monitoring data from non-glacial Arctic lakes, Cockburn and Lamoureux (2008) show that lacustrine suspended sediment fluxes mimic snow melt rates under a nival stream regime. We therefore contend that episodic snowmelt drove Late Holocene flooding in the Ymer catchment. Considering their coincidence with regional Neoglacial cooling (Fig. 8), it should be noted that Woo and Sauriol (1981) and Forbes and Lamoureux (2005) indicate that such melt events are most intense and prolonged in the Arctic during cool springs. Indeed, the highest-amplitude events around 3800 and 2450 cal. yr BP coincide with two established Greenland cold episodes (Fig. 8e) (Kobashi et al., 2017), the Bronze Age Cold Epoch (BACE, 3750–3450 cal. yr BP) and the Iron Age Cold Epoch (IACE, 2850–2250 cal. yr BP).

5.5. Little Ice Age glacier re-growth during the Medieval Warm Period (1200–0 cal. yr BP)

Unit 1 (0–35 cm, 1200 cal. yr BP-present) marks the first phase of fine-grained minerogenic lacustrine sedimentation since inferred deglaciation of the Ymer catchment around 9600–9500 cal. yr BP (Section 5.1). Following a shift towards silt-dominated clastic input around 1200 cal. BP (Fig. 8e), minerogenic indicators Ca, DBD and MS capture a sustained increase in dense minerogenic sedimentation from ~1000 cal. yr BP onwards (Fig. 8f). CT imagery of Fig. 6c reveal the rapidity of this transition. As previously stated (see Section 5.1), this sedimentary signature is diagnostic of glacial rock flour deposition (e.g. Leemann and Niessen, 1994; Peach and Perrie, 1975), and characterizes Ymer lake during a period of documented glacier activity in the catchment (Figs. 8e and f). Hence, unit 1 heralds a period of glacier reformation in the catchment. This interpretation is supported by a growing body of work indicating that the Late Holocene expansion of Greenland glaciers predate the accepted onset of the Little Ice Age (LIA: ~650–100 cal. yr BP) and coincides with the Medieval Warm period (MWP: ~1000–700 cal. yr BP) (Fig. 8). Locally, Hasholt (2000) provide a minimum age of 1435 ± 60 cal. yr BP for the Late Holocene advance of Mittivakkat glacier by radiocarbon-dating plant material on a now-exposed Nunatak (Figs. 2a and 8i). Also, Balascio et al. (2015) reconstruct a major advance of the nearby Kulusuk glacier at ~1200 cal. BP (Figs. 1c and 8g). Underlining the regional consistency of this glacier response, Lowell et al. (2013) and Miller et al. (2013) show that Istorvet Ice Cap near Scoresby Sund on central East Greenland had reformed by 1050 cal. yr BP (Figs. 1a and 8i). Complimenting this evidence by dating moraines fronting another ice cap in the same area, Levy et al. (2014) indicate that ice subsequently advanced until 740 cal. yr BP. Employing the same approach, Jomelli et al. (2016) reveal a similar glacier evolution on West Greenland, where Lyngmarks glacier on Disko Island had advanced towards its LIA maximum by ~800 cal. yr BP.

The climate forcing(s) mechanisms driving the pre-LIA expansion of mountain glaciers on Greenland remain debated. But based on the timing of glacier growth in the Ymer catchment, our findings challenge two often invoked causes - solar irradiance and volcanism: glacier formation after ~1200 cal. BP precedes a phase of frequent explosive volcanism between 675 and 650 cal. yr BP and a series of grand solar minima from ~900 cal. yr BP onwards that are often associated with the onset of the LIA in the North Atlantic (Jiang et al., 2015; Miller et al., 2012). Based on widespread foraminiferal evidence for strengthened advection of cold (ice-laden) polar waters on the East Greenland shelf after ~1.4 ka BP (Figs. 8a and b)(Perner et al., 2016; Perner et al., 2015), we postulate that changes in ocean circulation set the stage for glacier growth. Placing these findings in a wider context, Moros et al. (2006) report an increase in drift ice fluxes and Arctic foraminiferal abundances on the North Iceland Shelf, which is climatically linked to East Greenland (Jennings and Weiner, 1996). Complementing these findings, Wanamaker Jr et al. (2012) infer a shift towards Arctic-dominated water masses in the area after ~1200 cal. yr BP by reconstructing shifts in local reservoir age. Moreno-Chamarro et al. (2016) present a dynamical explanation for this pattern of change by invoking abrupt weakening of the Sub Polar Gyre (SPG) based on model simulations of pre-industrial climate. SPG weakening also provides a means of reconciling the time lag between the commonly used onset of the LIA, based on the expansion of European glaciers (Matthews and Briffa, 2005), and that of the presented Greenlandic precursor. As outlined by e.g. Larsen et al. (2013) and Young et al. (2015), SPG shifts, and their impact on North Atlantic Oscillation (NAO) phasing (Deshayes and Frankignoul, 2008), generating a temperature dipole across the North Atlantic. While spurring their formation and advance on Greenland, SPG weakening may simultaneously create unfavorable conditions for glaciers in Western Europe.

6. Conclusions

Using multiple lines of observational, physical, visual and geochemical proxy evidence and a robust ^{210}Pb and ^{14}C-based chronology, we resolved the Holocene evolution of Ymer Lake on Ammassalik Island in southeast Greenland at sub-centennial timescales. This multi-proxy approach allowed us to gain a process-based understanding of regime shifts in the lake sediment record. Integrated in a broader paleoclimate context, our findings reveal a climate history marked by three distinct threshold responses to regional Holocene climate transitions. The onset of lake sedimentation around 10 cal. ka BP provides a maximum age estimate for deglaciation that supports existing proxy and model evidence (Lecavalier et al., 2014; Long et al., 2008; Roberts et al., 2008). The catchment remained glaciated until ~9.5 cal. ka BP, when a combination of insolation-driven atmospheric and oceanic warming caused rapid retreat that culminated in a catastrophic Glacial Lake Outburst Flood (GLOF) (Andersen et al., 2004; Axford et al., 2017). After the Holocene optimum, characterized by subtle changes in minerogenic sedimentation with a distal glacial or an aeolian signature between 9.5 and 5 cal. ka BP, conditions shifted again. As temperatures decreased and the polar front migrated south during the regional inception of Neoglacial conditions (Jennings et al., 2011), lengthening seasonal lake ice coverage and shifting wind patterns allowed on-lake deposition of coarse avalanche deposits after 4.2 cal. ka BP. While evidence of avalanching continued to govern the record, the Late Holocene is interspersed with locally consistent flooding events during established Greenland cold episodes (Balascio et al., 2013; Kobashi et al., 2017). Finally, glaciers reformed in the catchment around 1.2 cal. ka BP amid a Greenland-wide advance during the MWP (Balascio et al., 2015; Jomelli et al., 2016; Lowell et al., 2013; Miller et al., 2013). While the causes of this LIA precursor remain unresolved, its timing and expression appear consistent with a southward movement of Arctic water masses linked to SPG weakening (Moreno-Chamarro et al., 2016; Moros et al., 2006; Perner et al., 2016; Wanamaker Jr et al., 2012; Young et al., 2015). These summarized findings demonstrate that Ymer Lake records major regional Holocene climate transitions: the deglaciation, Neoglacial cooling and the onset of pre-LIA glacier growth. This work directly links these climate changes to shifts in surface processes by characterizing the depositional signature of Ymer Lake sediments using an updated (CT, XRD) multi-proxy toolbox. In conclusion, this study showcases the capacity of Arctic lakes to sensitively capture changing climate signals.

Acknowledgements

This work was supported by an EU-Interact TA grant (GLEESP), the ECONORS fast-track initiative from the Centre for Climate Dynamics (SKD) at the Bjerknes Centre for Climate Research and the Research Council of Norway (NFR) through the Centre for Geobiology (CGB) (project 179560) and EARTHLAB (grant no. 226171). We thank Torgeir Røthe and Craig Frew for helping retrieve the studied sediment cores, Jordan Donn Holl for helping carry out lab analyses and Tor Einar Møller for his thorough proof-reading. Finally, we acknowledge Stein-Erik Lauritzen and Sverre Aksnes for measuring ^{210}Pb activity on dated sediment samples.

Declarations of interest

None.

References

Allen, P.A., 2008. From landscapes into geological history. Nature 451 (7176), 274–276.
Alonso-Garcia, M., Sierro, F.J., Flores, J.A., 2011. Arctic front shifts in the subpolar North Atlantic during the Mid-Pleistocene (800–400 ka) and their implications for ocean circulation. Palaeogeogr. Palaeoclimatol. Palaeoecol. 311 (3), 268–280.
Andersen, C., Koç, N., Jennings, A., Andrews, J.T., 2004. Nonuniform response of the major surface currents in the Nordic Seas to insolation forcing: Implications for the

Holocene climate variability. Paleoceanography 19 (2) (n/a-n/a).
Andresen, C.S., et al., 2012. Rapid response of Helheim Glacier in Greenland to climate variability over the past century. Nat. Geosci. 5 (1), 37–41.
Andresen, C., et al., 2013. Mid-to late-Holocene oceanographic variability on the Southeast Greenland shelf. The Holocene 23 (2), 167–178.
Anthony, R., 1977. Iron-rich rhythmically laminated sediments in Lake of the Clouds, northeastern Minnesota. Limnol. Oceanogr. 22 (1), 45–54.
Appleby, P., Oldfield, F., 1978. The calculation of lead-210 dates assuming a constant rate of supply of unsupported 210 Pb to the sediment. Catena 5 (1), 1–8.
Axford, Y., et al., 2017. Timing and magnitude of early to middle Holocene warming in East Greenland inferred from chironomids. Boreas 46 (4), 678–687.
BAARE, 1930. South coast of Angmagssalik Island. In: P53/43/138. Scott Polar Research Institute Cambridge.
Bakke, J., Nesje, A., Dahl, S.O., 2005. Utilizing physical sediment variability in glacier-fed lakes for continuous glacier reconstructions during the Holocene, northern Folgefonna, western Norway. The Holocene 15 (2), 161–176.
Bakke, J., et al., 2009. Rapid oceanic and atmospheric changes during the Younger Dryas cold period. Nat. Geosci. 2 (3), 202–205.
Bakke, J., et al., 2010. A complete record of Holocene glacier variability at Austre Okstindbreen, northern Norway: an integrated approach. Quat. Sci. Rev. 29 (9), 1246–1262.
Balascio, N.L., D'Andrea, W.J., Bradley, R.S., Perren, B.B., 2013. Biogeochemical evidence for hydrologic changes during the Holocene in a lake sediment record from Southeast Greenland. The Holocene 23 (10), 1428–1439.
Balascio, N.L., D'Andrea, W.J., Bradley, R., 2015. Glacier response to North Atlantic climate variability during the Holocene. Clim. Past 11 (12), 1587–1598.
Ballantyne, C.K., 2002. Paraglacial geomorphology. Quat. Sci. Rev. 21 (18), 1935–2017.
Benn, D., Evans, D.J., 2014. Glaciers and Glaciation. Routledge.
Bjørk, A.A., et al., 2012. An aerial view of 80 years of climate-related glacier fluctuations in southeast Greenland. Nat. Geosci. 5 (6), 427–432.
Blaauw, M., Christen, J.A., 2011. Flexible paleoclimate age-depth models using an autoregressive gamma process. Bayesian Anal. 6 (3), 457–474.
Blott, S.J., Pye, K., 2001. GRADISTAT: a grain size distribution and statistics package for the analysis of unconsolidated sediments. Earth Surf. Process. Landf. 26 (11), 1237–1248.
Briner, J.P., et al., 2016. Holocene climate change in Arctic Canada and Greenland. In: Quaternary Science Reviews.
Brown, L.C., Duguay, C.R., 2010. The response and role of ice cover in lake-climate interactions. Prog. Phys. Geogr. 34 (5), 671–704.
Cappelen, J., Laursen, E.V., Jørgensen, P.V., Kern-Hansen, C., 2011. DMI monthly climate data collection 1768-2010, Denmark, the Faroe Islands and Greenland. Tech. Rep. 05.
Carrivick, J.L., et al., 2013. Contemporary geomorphological activity throughout the proglacial area of an alpine catchment. Geomorphology 188, 83–95.
CEC, 2004. North American Environmental Atlas - Glaciers. (Ottawa, Ontario, Canada).
Christiansen, H.H., Murray, A.S., Mejdahl, V., Humlum, O., 1999. Luminescence dating of Holocene geomorphic activity on Ammassalik Island, SE Greenland. Quat. Sci. Rev. 18 (2), 191–205.
Cnudde, V., Boone, M.N., 2013. High-resolution X-ray computed tomography in geosciences: a review of the current technology and applications. Earth Sci. Rev. 123, 1–17.
Cockburn, J.M., Lamoureux, S.F., 2008. Hydroclimate controls over seasonal sediment yield in two adjacent high Arctic watersheds. Hydrol. Process. 22 (12), 2013–2027.
Coxsys, 2006. ITRAX Q-Spec 6.5.2 software manual. In: 17.
Croudace, I.W., Rindby, A., Rothwell, R.G., 2006. ITRAX: description and evaluation of a new multi-function X-ray core scanner. Special Publication-Geol. Soc. London 267, 51.
Cuven, S., Francus, P., Lamoureux, S.F., 2010. Estimation of grain size variability with micro X-ray fluorescence in laminated lacustrine sediments, Cape Bounty, Canadian High Arctic. J. Paleolimnol. 44 (3), 803–817.
Dahl-Jensen, D., et al., 1998. Past temperatures directly from the Greenland ice sheet. Science 282 (5387), 268–271.
Davies, S.J., Lamb, H.F., Roberts, S.J., 2015. Micro-XRF core scanning in palaeolimnology: recent developments, Micro-XRF studies of sediment cores. Springer 189–226.
Davin, S.H., 2013. 7700 Years of Holocene Climatic Variability in Sermilik Valley. Southeast Greenland Inferred From Lake Sediments.
Dean Jr, W.E., 1974. Determination of carbonate and organic matter in calcareous sediments and sedimentary rocks by loss on ignition: comparison with other methods. J. Sediment. Res. 44 (1).
Deshayes, J., Frankignoul, C., 2008. Simulated variability of the circulation in the North Atlantic from 1953 to 2003. J. Clim. 21 (19), 4919–4933.
DeVries-Zimmerman, S., Fisher, T.G., Hansen, E.C., Dean, S., Björck, S., 2014. Sand in lakes and bogs in Allegan County, Michigan, as a proxy for eolian sand transport. Geol. Soc. Am. Spec. Pap. 508, SPE508–07.
Dorschel, B., Jakobsson, M., 2016. General Bathymetric Chart of the Oceans–GEBCO–A Look at the World from an ocean's Perspective, ESA and EC. Copernicus Sentinel 2.
Fetterer, F., Knowles, K., Meier, W., Savoie, M., 2016. Sea ice index, version 2. In: N.N.S.a.I.D. Center, (Boulder, Colorado (USA)).
Forbes, A.C., Lamoureux, S.F., 2005. Climatic controls on streamflow and suspended sediment transport in three large middle arctic catchments, Boothia peninsula, Nunavut, Canada. Arct. Antarct. Alp. Res. 37 (3), 304–315.
Fouinat, L., et al., 2017. A new CT scan methodology to characterize a small aggregation gravel clast contained in a soft sediment matrix. Earth Surf. Dynam. 5 (1), 199–209.
Gelaro, R. et al., 2017. The Modern-Era Retrospective Analysis for Research and Applications, Version 2 (MERRA-2). J. Clim.(2017).
Hammer, Ø., 2013. PAST Paleontological Statistics Version 3.0: Reference Manual. University of Oslo.
Hasholt, B., 2000. Evidence of a warmer climate around AD 600, Mittivakkat Glacier. South East Greenland. Geografisk Tidsskrift 100.
Hasholt, B., Liston, G.E., Knudsen, N.T., 2003. Snow-distribution modelling in the Ammassalik region, south east Greenland. Hydrol. Res. 34 (1–2), 1–16.
Howat, I., Negrete, A., Smith, B., 2014. The Greenland ice mapping project (GIMP) land classification and surface elevation data sets. Cryosphere 8 (4), 1509–1518.
Humlum, O., Christiansen, H.H., 2008. Geomorphology of the Ammassalik Island, SE Greenland. Geografisk Tidsskrift-Danish J. Geogr. 108 (1), 5–20.
Huybers, P., 2006. Early Pleistocene glacial cycles and the integrated summer insolation forcing. Science 313 (5786), 508–511.
ICCD, 2007. PDF-2, Database Sets 1–45. International Centre for Diffraction Data.
IPCC, 2013. In: Tignor, K., Allen, M., Boschung, S.K., Nauels, J., Xia, A., Bex V, Y., Midgley, P.M. (Eds.), The physical science basis. Contribution of working group I to the fifth assessment report of the intergovernmental panel on climate change, pp. 1535.
Jakobsen, B.H., Fredskild, B., Pedersen, J.B.T., 2008. Holocene changes in climate and vegetation in the Ammassalik area, East Greenland, recorded in lake sediments and soil profiles. Geografisk Tidsskrift-Danish J. Geogr. 108 (1), 21–50.
Jeffries, MO, Richter-Menge, J, Overland, JE, 2015. Arctic Report Card 2015.
Jennings, A.E., Weiner, N.J., 1996. Environmental change in eastern Greenland during the last 1300 years: evidence from foraminifera and lithofacies in Nansen Fjord, 68 N. The Holocene 6 (2), 179–191.
Jennings, A., Andrews, J., Wilson, L., 2011. Holocene environmental evolution of the SE Greenland shelf north and south of the Denmark Strait: Irminger and East Greenland current interactions. Quat. Sci. Rev. 30 (7–8), 980–998.
Jiang, H., et al., 2015. Solar forcing of Holocene summer sea-surface temperatures in the northern North Atlantic. Geology 43 (3), 203–206.
Jomelli, V., et al., 2016. Paradoxical cold conditions during the medieval climate anomaly in the Western Arctic. Sci. Rep. 6, 32984.
Juggins, S., 2009. Rioja: analysis of quaternary science data. R package version 0. pp. 5–6.
Kalsbeek, F., 1989. Geology of the Ammassalik Region, South-East Greenland, 146. Grønlands geologiske undersøgelse.
Karlén, W., 1976. Lacustrine sediments and tree-limit variations as indicators of Holocene climatic fluctuations in Lappland, northern Sweden. Geografiska Annaler. Series A. Physical Geography 1–34.
Klein Tank, A., et al., 2002. Daily dataset of 20th-century surface air temperature and precipitation series for the European climate assessment. Int. J. Climatol. 22 (12), 1441–1453.
Kobashi, T., et al., 2017. Volcanic influence on centennial to millennial Holocene Greenland temperature change. Sci. Rep. 7 (1), 1441.
Kolb, J., 2014. Structure of the Palaeoproterozoic Nagssugtoqidian Orogen, south-East Greenland: model for the tectonic evolution. Precambrian Res. 255, 809–822.
Lamoureux, S., Gilbert, R., 2004a. Physical and chemical properties and proxies of high latitude lake sediments. In: Smol, J., Pienitz, R., Douglas, M.V. (Eds.), Long-Term Environmental Change in Arctic and Antarctic Lakes. Developments in Paleoenvironmental Research. Springer, Netherlands, pp. 53–87.
Lamoureux, S.F., Gilbert, R., 2004b. A 750-yr record of autumn snowfall and temperature variability and winter storminess recorded in the varved sediments of Bear Lake, Devon Island, Arctic Canada. Quat. Res. 61 (2), 134–147.
Larsen, D.J., Miller, G.H., Geirsdóttir, Á., 2013. Asynchronous little ice age glacier fluctuations in Iceland and European alps linked to shifts in subpolar North Atlantic circulation. Earth Planet. Sci. Lett. 380 (0), 52–59.
Last, W.M., Smol, J.P., 2002. Tracking Environmental Change Using Lake Sediments. Tracking Environmental Change Using Lake Sediments. Springer.
Lecavalier, B.S., et al., 2014. A model of Greenland ice sheet deglaciation constrained by observations of relative sea level and ice extent. Quat. Sci. Rev. 102, 54–84.
Leemann, A., Niessen, F., 1994. Varve formation and the climatic record in an Alpine proglacial lake: calibrating annually-laminated sediments against hydrological and meteorological data. The Holocene 4 (1), 1–8.
Levy, L.B., et al., 2014. Holocene fluctuations of Bregne ice cap, Scoresby Sund, east Greenland: a proxy for climate along the Greenland ice sheet margin. Quat. Sci. Rev. 92, 357–368.
Liermann, S., Beylich, A.A. and van Welden, A., 2012. Contemporary suspended sediment transfer and accumulation processes in the small proglacial Sætrevatnet sub-catchment, Bødalen, western Norway. Geomorphology, 167–168(0), 91–101.
Long, A.J., et al., 2008. Late Weichselian relative sea-level changes and ice sheet history in southeast Greenland. Earth Planet. Sci. Lett. 272 (1), 8–18.
Lowell, T.V., et al., 2013. Late Holocene expansion of Istorvet ice cap, Liverpool Land, east Greenland. Quat. Sci. Rev. 63, 128–140.
Luckman, B., 1975. Drop stones resulting from snow-avalanche deposition on lake ice. J. Glaciol. 14 (70), 186–188.
Marcott, S.A., Shakun, J.D., Clark, P.U., Mix, A.C., 2013. A reconstruction of regional and global temperature for the past 11,300 years. Science 339 (6124), 1198–1201.
Matthews, J.A., Briffa, K.R., 2005. The 'little ice age': re-evaluation of an evolving concept. Geogr. Ann. 87 (1), 17–36.
Mernild, S.H., Hasholt, B., 2006. Climatic control on river discharge simulations, Mittivakkat glacier catchment, Ammassalik Island, SE Greenland*. Hydrol. Res. 37 (4–5), 327–346.
Mernild, S.H., et al., 2008. Climate, glacier mass balance and runoff (1993–2005) for the Mittivakkat Glacier catchment, Ammassalik Island, SE Greenland, and in a long term perspective (1898–1993). Hydrol. Res. 39 (4), 239–256.
Mernild, S.H., et al., 2011. Increasing mass loss from Greenland's Mittivakkat Gletscher. Cryosphere 5 (2), 341–348.
Miller, G.H., et al., 2012. Abrupt onset of the little ice age triggered by volcanism and sustained by sea-ice/ocean feedbacks. Geophys. Res. Lett. 39 (2).

Miller, G.H., et al., 2013. Substantial agreement on the timing and magnitude of late Holocene ice cap expansion between East Greenland and the eastern Canadian Arctic: a commentary on Lowell et al., 2013. Quat. Sci. Rev. 77, 239–245.
Moffa-Sánchez, P., Born, A., Hall, I.R., Thornalley, D.J., Barker, S., 2014. Solar forcing of North Atlantic surface temperature and salinity over the past millennium. Nat. Geosci. 7 (4), 275–278.
Moreno-Chamarro, E., Zanchettin, D., Lohmann, K., Jungclaus, J.H., 2016. An abrupt weakening of the subpolar gyre as trigger of little ice age-type episodes. Clim. Dyn. 1–18.
Moros, M., Andrews, J.T., Eberl, D.D., Jansen, E., 2006. Holocene history of drift ice in the northern North Atlantic: evidence for different spatial and temporal modes. Paleoceanography 21 (2).
NOAA, 2012. 4km AVHRR Pathfinder v5.0 Global Day-night sea surface temperature monthly and yearly averages, 1985–2009. In: N.O.D. Center.
Oltmanns, M., Straneo, F., Moore, G., Mernild, S.H., 2014. Strong downslope wind events in Ammassalik, southeast Greenland. J. Clim. 27 (3), 977–993.
Oswald, W.W., et al., 2005. Effects of sample mass and macrofossil type on radiocarbon dating of arctic and boreal lake sediments. The Holocene 15 (5), 758–767.
Paillard, D., Labeyrie, L., Yiou, P., 1996. Analyseries 1.0: a Macintosh software for the analysis of geographical time-series. Eos 77, 379.
Peach, P.A., Perrie, L.A., 1975. Grain-size distribution within glacial varves. Geology 3 (1), 43–46.
Perner, K., Moros, M., Lloyd, J.M., Jansen, E., Stein, R., 2015. Mid to late Holocene strengthening of the East Greenland Current linked to warm subsurface Atlantic water. Quat. Sci. Rev. 129, 296–307.
Perner, K., Jennings, A.E., Moros, M., Andrews, J.T., Wacker, L., 2016. Interaction between warm Atlantic-sourced waters and the East Greenland current in northern Denmark Strait (68° N) during the last 10 600 cal a BP. J. Quat. Sci. 31 (5), 472–483.
Poppe, L., Paskevich, V., Hathaway, J., Blackwood, D., 2001. A laboratory manual for X-ray powder diffraction. US Geol. Survey Open-File Rep. 1 (041), 1–88.
RCoreTeam, 2014. R: a language and environment for statistical computing. Vienna, Austria: R Foundation for Statistical Computing; 2012. Open access available at. http://cran (r-project. org).
Reimer, P.J., et al., 2013. IntCal13 and Marine13 radiocarbon age calibration curves 0–50,000 years cal BP. Radiocarbon 55 (4), 1869–1887.
Roberts, D.H., Long, A.J., Schnabel, C., Freeman, S., Simpson, M.J., 2008. The deglacial history of southeast sector of the Greenland ice sheet during the last glacial maximum. Quat. Sci. Rev. 27 (15), 1505–1516.
Rollison, H.R., 1993. Using Geochemical Data: Evaluation, Presentation. Longan Scientific and Technical Press, Interpretation. New York.
Rosenblum, S., Brownfield, I.K., 2000. Magnetic Susceptibilities of Minerals. (Citeseer).
Ryżak, M., Bieganowski, A., 2011. Methodological aspects of determining soil particle-size distribution using the laser diffraction method. J. Plant Nutr. Soil Sci. 174 (4), 624–633.
Sandgren, P., Snowball, I., 2002. Application of mineral magnetic techniques to paleolimnology. Tracking Environ. Change using Lake Sediments 217–237.
Schjøth, F., et al., 2012. Campaign to map the bathymetry of a major Greenland fjord. EOS Trans. Am. Geophys. Union 93 (14), 141–142.
Serreze, M.C., Barry, R.G., 2011. Processes and impacts of Arctic amplification: a research synthesis. Glob. Planet. Chang. 77 (1–2), 85–96.
Smol, J.P., et al., 2005. Climate-driven regime shifts in the biological communities of arctic lakes. PNAS 102 (12), 4397–4402.
Straneo, F., et al., 2010. Rapid circulation of warm subtropical waters in a major glacial fjord in East Greenland. Nat. Geosci. 3 (3), 182–186.
Sundqvist, H., et al., 2014. Arctic Holocene proxy climate database–new approaches to assessing geochronological accuracy and encoding climate variables. Clim. Past Discuss. 10 (1), 1–63.
van der Bilt, W.G.M., Bakke, J., Vasskog, K., Røthe, T., Støren, E.W.N., 2016. Glacier-fed lakes as palaeoenvironmental archives. Geol. Today 32 (6), 213–218.
van der Bilt, W.G.M., et al., 2017. Late Holocene glacier reconstruction reveals retreat behind present limits and two-stage Little Ice Age on subantarctic South Georgia. J. Quat. Sci. 32 (6), 888–901.
Vasskog, K., et al., 2011. A Holocene record of snow-avalanche and flood activity reconstructed from a lacustrine sedimentary sequence in Oldevatnet, western Norway. The Holocene 11 (4), 597–614 (0959683610391316).
Wanamaker Jr, A.D., et al., 2012. Surface changes in the North Atlantic meridional overturning circulation during the last millennium. Nat. Commun. 3, 899.
Wanner, H., 2014. Holocene Climate. Glob. Environ. Chang. 55–59.
Wanner, H., Solomina, O., Grosjean, M., Ritz, S.P., Jetel, M., 2011. Structure and origin of Holocene cold events. Quat. Sci. Rev. 30 (21), 3109–3123.
Woo, M.-K., Sauriol, J., 1981. Effects of snow jams on fluvial activities in the High Arctic. Phys. Geogr. 2 (1), 83–98.
Xu, M., Bogen, J., Wang, Z., Bønsnes, T.E., Gytri, S., 2015. Pro-glacial lake sedimentation from jökulhlaups (GLOF), Blåmannsisen, northern Norway. Earth Surf. Process. Landf. 40 (5), 654–665.
Young, N.E., Schweinsberg, A.D., Briner, J.P., Schaefer, J.M., 2015. Glacier maxima in Baffin Bay during the medieval warm period coeval with Norse settlement. Sci. Adv. 1 (11), e1500806.
Zhang, G., Yao, T., Xie, H., Wang, W., Yang, W., 2015. An inventory of glacial lakes in the third pole region and their changes in response to global warming. Glob. Planet. Chang. 131, 148–157.